

Article

Preparation of Composite Electrodes for All-Solid-State Batteries Based on Sulfide Electrolytes: An Electrochemical Point of View

Sara Giraldo ¹, Koki Nakagawa ², Ferley A. Vásquez ¹, Yuta Fujii ², Yongming Wang ³, Akira Miura ⁴, Jorge A. Calderón ^{1,*}, Nataly C. Rosero-Navarro ^{4,*} and Kiyoharu Tadanaga ⁴

¹ Centro de Investigación, Innovación y Desarrollo de Materiales (CIDEVAT), Universidad de Antioquia, Street 70 # 52-21, Medellín 050010, Colombia; sara.giraldom@udea.edu.co (S.G.); ferley.vasquez@udea.edu.co (F.A.V.)

² Graduate School of Chemical Science and Engineering, Hokkaido University, Kita 13, Nishi 8, Sapporo 060-8628, Japan; k.nakagawa@frontier.hokudai.ac.jp (K.N.); fujii.yuta@frontier.hokudai.ac.jp (Y.F.)

³ Creative Research Institution (CRIS), Hokkaido University, Kita 21, Nishi 10, Sapporo 001-0021, Japan; wang@eng.hokudai.ac.jp

⁴ Division of Applied Chemistry, Hokkaido University, Sapporo 060-8628, Japan; amiura@eng.hokudai.ac.jp (A.M.); tadanaga@eng.hokudai.ac.jp (K.T.)

* Correspondence: andres.calderon@udea.edu.co (J.A.C.); rosero@eng.hokudai.ac.jp (N.C.R.-N.)



Citation: Giraldo, S.; Nakagawa, K.; Vásquez, F.A.; Fujii, Y.; Wang, Y.; Miura, A.; Calderón, J.A.; Rosero-Navarro, N.C.; Tadanaga, K. Preparation of Composite Electrodes for All-Solid-State Batteries Based on Sulfide Electrolytes: An Electrochemical Point of View. *Batteries* **2021**, *7*, 77. <https://doi.org/10.3390/batteries7040077>

Academic Editor: Mathieu Doucet

Received: 2 September 2021

Accepted: 8 November 2021

Published: 11 November 2021

Publisher's Note: MDPI stays neutral with regard to jurisdictional claims in published maps and institutional affiliations.



Copyright: © 2021 by the authors. Licensee MDPI, Basel, Switzerland. This article is an open access article distributed under the terms and conditions of the Creative Commons Attribution (CC BY) license (<https://creativecommons.org/licenses/by/4.0/>).

Abstract: All-solid-state batteries (ASSBs) are a promising response to the need for safety and high energy density of large-scale energy storage systems in challenging applications such as electric vehicles and grid integration. ASSBs based on sulfide solid electrolytes (SEs) have attracted much attention because of their high ionic conductivity and wide electrochemical windows of the sulfide SEs. Here, we study the electrochemical performance of ASSBs using composite electrodes prepared via two processes (simple mixture and solution processes) and varying the ionic conductor additive (80Li₂S·20P₂S₅ and argyrodite-type Li₆PS₅Cl). The composite electrodes consist of lithium-silicate-coated LiNi_{1/3}Mn_{1/3}Co_{1/3}O₂ (NMC), a sulfide SE, and carbon additives. The charge-transfer resistance at the interface of the solid electrolyte and NMC is the main parameter related to the ASSB's status. This value decreases when the composite electrodes are prepared via a solution process. The lithium silicate coating and the use of a high-Li-ion additive conductor are also important to reduce the interfacial resistance and achieve high initial capacities (140 mAh g⁻¹).

Keywords: all-solid-state batteries; sulfide solid electrolyte; solution process; electrochemical impedance analysis

1. Introduction

Lithium-ion batteries offer the highest volumetric and gravimetric energy density among currently used electrochemical storage systems. Thus, such batteries have widely been used as power sources for portable devices such as computers, mobile phones, and digital cameras; recently, these batteries have also been extensively used as energy storage devices for electric vehicles and substations. Nevertheless, the development of the electric automobile industry has prompted an intensive search for improving lithium-ion batteries to obtain a high energy density in order to deliver high currents [1,2]. All-solid-state batteries (ASSBs) offer high energy density, accompanied by solutions for critical safety concerns. However, these devices still have many unsolved problems that keep them from commercialization, such as interfacial instability, lithium dendrite formation, and lack of mechanical integrity during cycling [3,4].

Among solid electrolytes (SEs), sulfide-based SEs such as glass-ceramics Li₂S-P₂S₅ binary systems, argyrodite-type Li₆PS₅X (X = Br, Cl, I), and LISICON-type Li₁₀GeP₂S₁₂

(LGPS) exhibit high lithium-ion conductivities up to 10 mS cm^{-1} and wide electrochemical windows (10 V). The combination of high ionic conductivity and mechanical properties (plasticity) of sulfide SEs make them a promising alternative for next-generation batteries [3]. Sulfide-based ASSBs have great potential to reach competitive energy densities of over 350 Wh kg^{-1} when coupled with high-energy cathodes and lithium metal anodes [4,5]. High-potential oxide cathode materials (e.g., LiCoO_2 , $\text{Li}_{4/3-x}\text{Ni}^{2+}_x\text{Mn}^{4+}_{2/3-x}\text{Co}^{3+}_x\text{O}_2$, NMC) and sulfide SEs are dissimilar materials; therefore, the chemical and electrochemical interaction between them generates an interfacial layer with high internal resistance that limits the power density and electrochemical performance of the battery [6]. The chemical reaction between oxide cathode materials and sulfide solid electrolytes occurs via the solid–solid interface [7,8]. The coexistence of elements belonging to both oxide cathode and sulfide solid electrolytes—such as S, P, and Co—has been observed in the interfacial layer [9,10], indicating that an interdiffusion process of such elements takes place during battery cycling. This interfacial layer is mostly ionically insulating (e.g., cobalt sulfides), which is one reason for the high interfacial resistance. In this sense, lithium-based oxide coatings (LiNbO_3 , LiAlO_2 , $\text{Li}_4\text{Ti}_5\text{O}_{12}$, and Li_3PO_4) on cathode materials are used to reduce the interfacial resistance generated by the chemical reaction layers (blocking interdiffusion). The coatings are also expected to diminish the effect of interfacial potential, facilitating the lithium transport (space-charge). These have proven to be rather effective in the enhancement of the rate capability and capacity retention of the ASSBs [6,9–16].

On the other hand, the preparation of composite electrodes with more intimate contacts between active materials and sulfide SEs is also crucial to achieving low interfacial resistance and, therefore, to enhancing the electrochemical performance of the ASSB. Typically, composite electrodes consist of a mixture of active material particles with the sulfide SE and/or carbon additives to improve ionic and electronic conduction paths to the active material. Recently, the liquid-phase process has proven to be a simple procedure that can effectively enhance the solid–solid contact through the composite electrode layer, resulting in a high initial capacity [17–26]. In this process, the active material and additive particles are immersed in a sulfide SE solution, and then particles of the active materials are covered with a layer-type sulfide SE after solvent removal. Although different composite electrodes have been fabricated using solution processes, the key parameters that affect the electrochemical performance of the ASSBs are not fully understood. Electrochemical impedance analysis is a powerful tool that is expected to evaluate the large-scale properties of the ASSB via the interpretation of internal cell resistances. This information could guide how ASSB properties such as capacity, cycle life, and performance can be improved [27].

In this work, composite electrodes containing lithium silicate (LS) [28,29]-coated $\text{LiNi}_{1/3}\text{Mn}_{1/3}\text{Co}_{1/3}\text{O}_2$ (NMC), a sulfide solid electrolyte, and carbon additives (vapor-grown carbon fiber (VGCF)) were prepared via a simple mixture and solution process. The effect of the SE type and ionic conductivity of the sulfide SE into the composite electrode on the electrochemical performance of the all-solid-state batteries was investigated. Particularly, changes in the internal resistances of the batteries using electrochemical impedance are discussed. The results suggest that intimate contact, obtained during the solution process, was the key to enhancing the electrochemical performance of the batteries. The ionic conductivity of the sulfide solid electrolyte around $10^{-5} \text{ S}\cdot\text{cm}^{-1}$ provides sufficient ionic percolation through the composite electrode, achieving high initial capacities and allowing their use at high potentials up to 5 V vs. Li. The impedance analysis suggests that the charge-transfer resistance between the solid electrolyte and the electrode materials (interfacial reactions) is the main parameter related to the global vision of the ASSB's status, and provides crucial information to predict the expected electrochemical performance of the cell.

2. Results and Discussion

Figure 1 illustrates the processes used for the preparation of the composite electrodes (details in Section 3). The simple mixture process (Figure 1a) consists of the mixture of the

LS-coated NMC, VGCF, and sulfide electrolyte in a mortar for few minutes. In the solution process (Figure 1b), LS-coated NMC is dispersed in a solution of the solid electrolyte, and then the composite electrode is obtained after solvent removal. The ionic conductivities of the sulfide solid electrolytes used to prepare the composite electrodes are summarized in Table 1. Both composite electrodes were evaluated in ASSLBs using $75\text{Li}_2\text{S}\text{-}25\text{P}_2\text{S}_5$ as a solid electrolyte separator ($10^{-4}\text{ S}\cdot\text{cm}^{-1}$) and Li-In alloy as an anode.

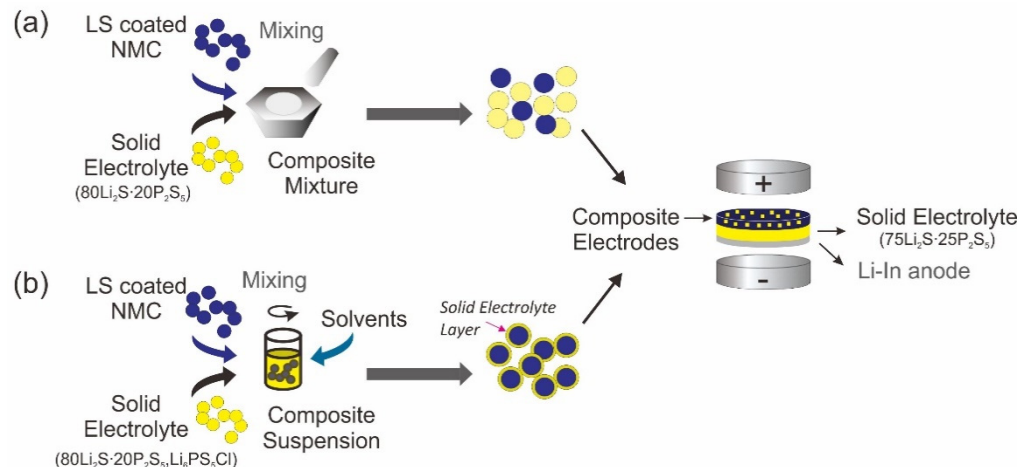


Figure 1. Processes used to prepare composite electrodes: (a) simple mixture; (b) solution process. Carbon additive VGCF is not illustrated to facilitate the explanation.

Table 1. Ionic conductivity of the sulfide solid electrolytes (details in Section 3).

Sulfide Solid Electrolyte Composition	Process	Ionic Conductivity $\text{S}\cdot\text{cm}^{-1}$ at 25°C
$80\text{Li}_2\text{S}\text{-}20\text{P}_2\text{S}_5$	MM ¹	9×10^{-5}
$80\text{Li}_2\text{S}\text{-}20\text{P}_2\text{S}_5$	SP ²	5×10^{-7}
$\text{Li}_6\text{PS}_5\text{Cl}$ (LPSCl)	SP ²	4×10^{-5}

¹ Mechanical milling; ² solution process (dissolution–precipitation).

Figure 2a,b show scanning electron microscopy (SEM) images of the pristine and LS-coated NMC particles, respectively. The morphology of NMC particles—a hemispherical primary particle of ca. $5\text{ }\mu\text{m}$ containing secondary particles of around $1\text{ }\mu\text{m}$ —remains unchanged after LS coating deposition. Figure 2c shows X-ray diffraction (XRD) patterns of the LS powder at 350°C . The crystallization of the lithium silicate to the Li_2SiO_3 orthorhombic phase with the $\text{Cmc}2_1$ space group (ICSD #853) was observed after 2 h of heat treatment. Therefore, the LS coating applied to the NMC particles was heated at 350°C for 0.5 h to obtain an amorphous coating [29]. Figure 2d–f show transmission electron microscopy (TEM) images of LS-coated NMC particles obtained from three batches (hereafter referred to as B1, B2, and B3). The LS coating achieves an average thickness of around 9 nm, with a variation between 5 and 14 nm. The variation in thickness arises from the tortuosity of the NMC microstructure and the difficulty in homogeneously covering the particle surface during the deposition. The effectiveness of the inorganic coating thickness in preventing side reactions between the electrode and electrolyte varies based on the material; however, a few nanometers have proven to be sufficient to reduce the interfacial resistance during the battery's cycling. For instance, LiNbO_3 -coated LiCoO_2 with a thickness of 8–12 nm and $\text{Li}_4\text{Ti}_5\text{O}_{15}$ coating of 5 nm have both been used [30].

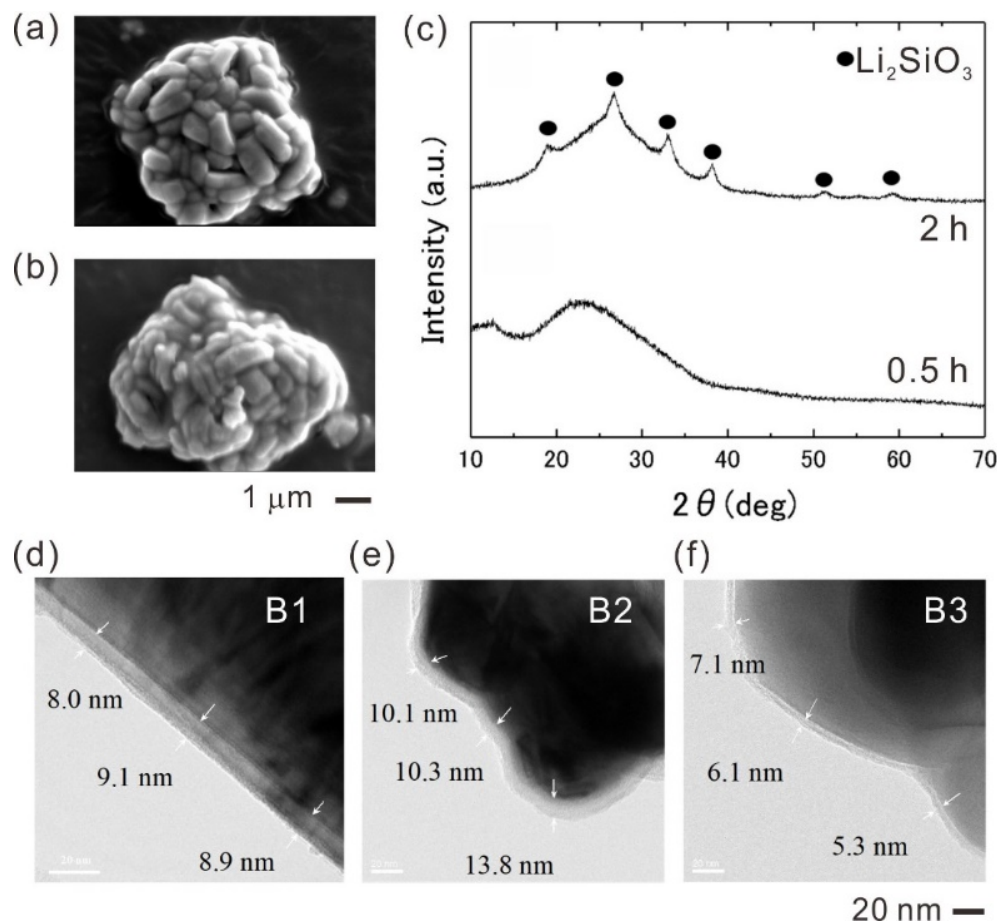


Figure 2. SEM images of the (a) pristine NMC and (b) LS-coated NMC particles. (c) X-ray diffraction (XRD) patterns of the lithium silicate at 350 °C. (d–f) TEM images of the LS-coated NMC particles from 3 batches.

Figure 3a,b show SEM–EDS (energy-dispersive spectroscopy) analysis of composite electrodes using an 80Li₂S·20P₂S₅ solid electrolyte prepared via simple mixture and solution processes, respectively. Clear segregation of LS-coated NMC and solid electrolyte particles was observed in the composite electrode obtained via a simple mixture (Figure 3a). In contrast, a homogeneous distribution of the sulfide solid electrolyte on the LS-coated NMC particles was observed in the composite electrode obtained via the solution process (Figure 3b).

Figure 4 shows the first charge-discharge curves of the all-solid-state cells using a composite electrode with 80Li₂S·20P₂S₅ solid electrolyte prepared by (a) simple mixture and (b) solution processes. The initial average capacity of the composite electrodes prepared by simple mixture achieves 60 mAh g⁻¹, while that obtained by solution process achieves 80 mAh g⁻¹ (without considering the composite electrode with LS-uncoated NMC). The enhancement of the initial capacity in the composite electrodes obtained by the solution process is attributed to the better solid-solid contacts between electrode and electrolyte (verified by SEM-EDS analysis, Figure 3b). Despite this improvement in the initial capacity, the value is still lower than the theoretical capacity (275 mAh g⁻¹) and reversibly accessible capacity (160 mAh g⁻¹) [31]. Moreover, the composite electrodes prepared by the solution process seem to show a wide variation (low reproducibility), including the high initial capacity of the composite electrode using LS-uncoated NMC (100 mAh g⁻¹).

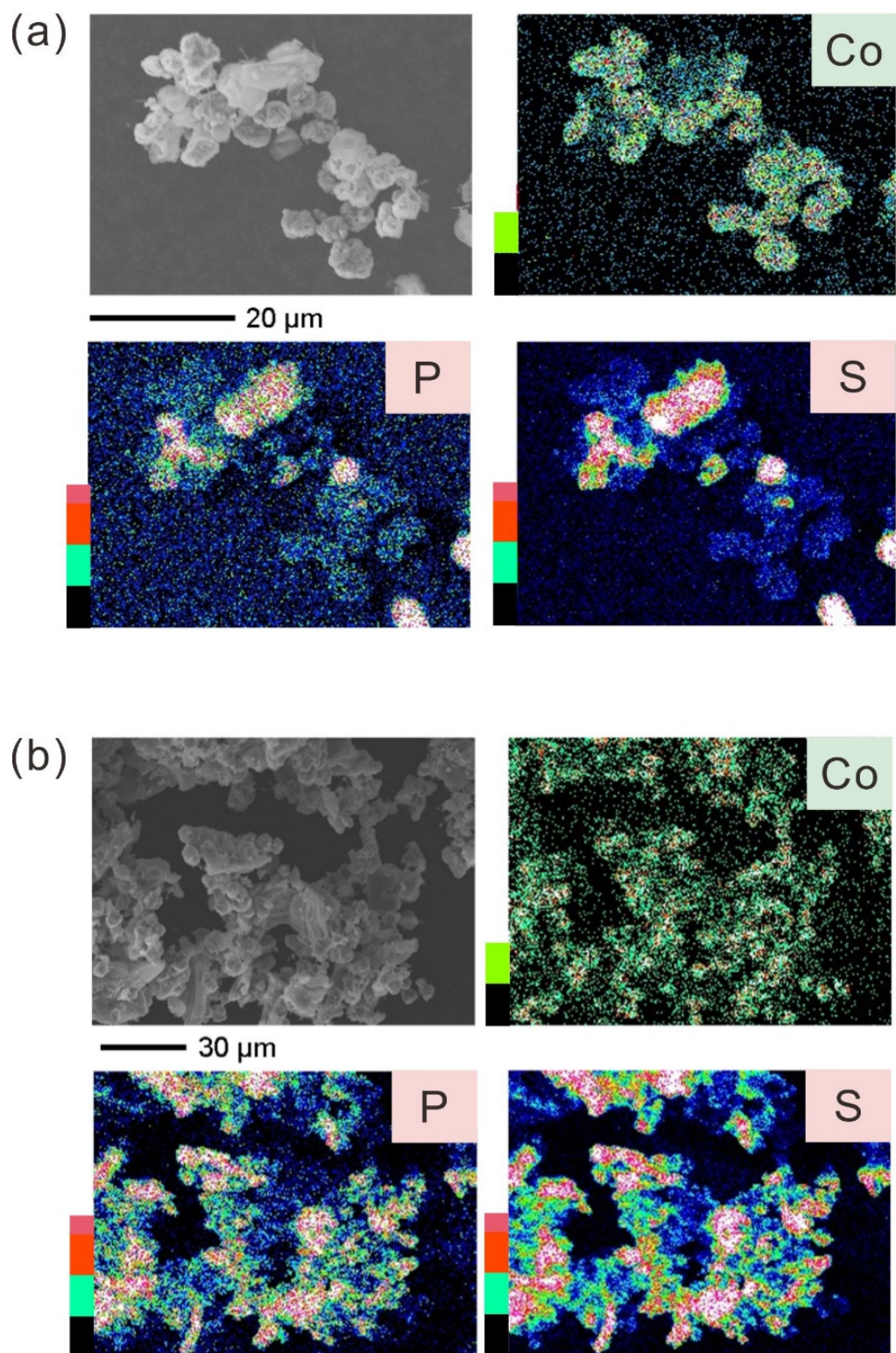


Figure 3. SEM–EDS analysis of composite electrodes prepared via (a) simple mixture and (b) solution processes using 80Li₂S–20P₂S₅ solid electrolytes. Elemental mappings for Co, P, and S are included. The color bar at the left-hand side corresponds to the intensity of the signal during the scanning acquisition.

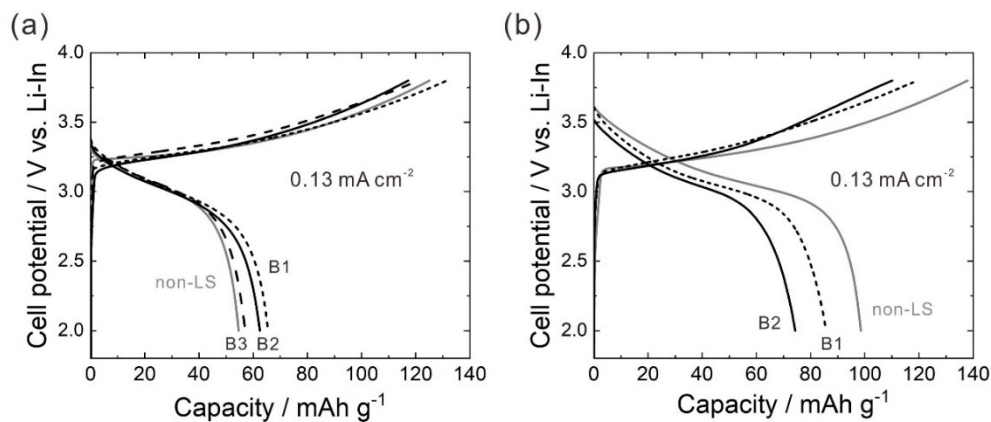


Figure 4. First charge–discharge curves of the all-solid-state cells using composite electrodes with 80Li₂S·20P₂S₅ solid electrolytes prepared via (a) simple mixture and (b) solution processes at 2.0 to 3.8 V vs. Li–In alloy (2.6 to 4.2 V vs. Li).

Figure 5 shows the impedance spectra of ASSBs using composite electrodes with 80Li₂S·20P₂S₅ SEs prepared via simple mixture and solution processes. The impedance spectra show similar contributions for both composite electrodes. However, it should be noted that the total internal resistance of the cell using composite electrodes prepared via simple mixture procedure ($1200\ \Omega$) was almost the double that of the cell using electrodes prepared via solution processes ($600\ \Omega$). In both cases, the total internal resistance of non-LS NMC was higher than that of the coated version (with the exception of B2 of the solution process, in which the total internal resistance was similar). Four characteristic frequencies can be identified in the Bode plot, with an equal number of resistance components, as shown in the Nyquist plot. An incomplete semicircle observed at high frequencies (>500 kHz) is related to the solid electrolyte (R_{SE}) [29]. At intermediate frequencies, two coupled capacitive semicircles are observed: the small semicircle at high–intermediate frequencies (10–30 kHz) is related to the solid electrolyte grain boundary (SE-GB); the semicircle at low–intermediate frequencies (100–300 Hz) is related to the interfacial resistance between the solid electrolyte and the cathode material ($R_{SE/Cat}$), in parallel with the interfacial capacitance. The semicircle at low frequencies (1–10 Hz) is due to the interfacial resistance between the solid electrolyte and the anode, in parallel with the interfacial capacitance [18].

The solid lines in Figure 5a–d correspond to the fitting results using the equivalent circuit in Figure 5e, and the fitting results are summarized in Table 2. Please note that the equivalent circuit for fitting non-LS in Figure 5a and B1 in Figure 5b uses only a resistance (R_{SE}) instead of an $R_{SE} \parallel CPSE$ element, because of the absence of information at high frequencies. The effective capacitance ($C_{eff.}$) is calculated from the pseudocapacitance (ϕ) and exponential factor (α) of the CP element, as described by Hirschorn et al. [31]. T is the characteristic time of the associated process. The R_{SE} and R_{SE-GB} exhibit similar values to those reported in the literature (~100–200 Ω) [29,32]. The R_{SE}/An is higher than reported values for the Li–In alloy (50–80 Ω) [29], which is associated with a possible overlapping with an additional resistance contribution. This contribution may be related to the cathode composite electrode, since the regimen of the frequency is close between both the cathode and anode interfaces. The data variation is associated with the experimental variation during battery assembly and batch/composite electrode preparation [33]. The largest resistance contribution in the impedance spectra corresponds to $R_{SE/Cat}$ [29,34], which is visibly reduced with the use of the LS protective coating, proving that the LS coating is effective at blocking the initial interfacial reactions. A significant reduction in the $R_{SE/Cat}$ was observed when the solution process was used to prepare the composite electrodes at more than $300\ \Omega$.

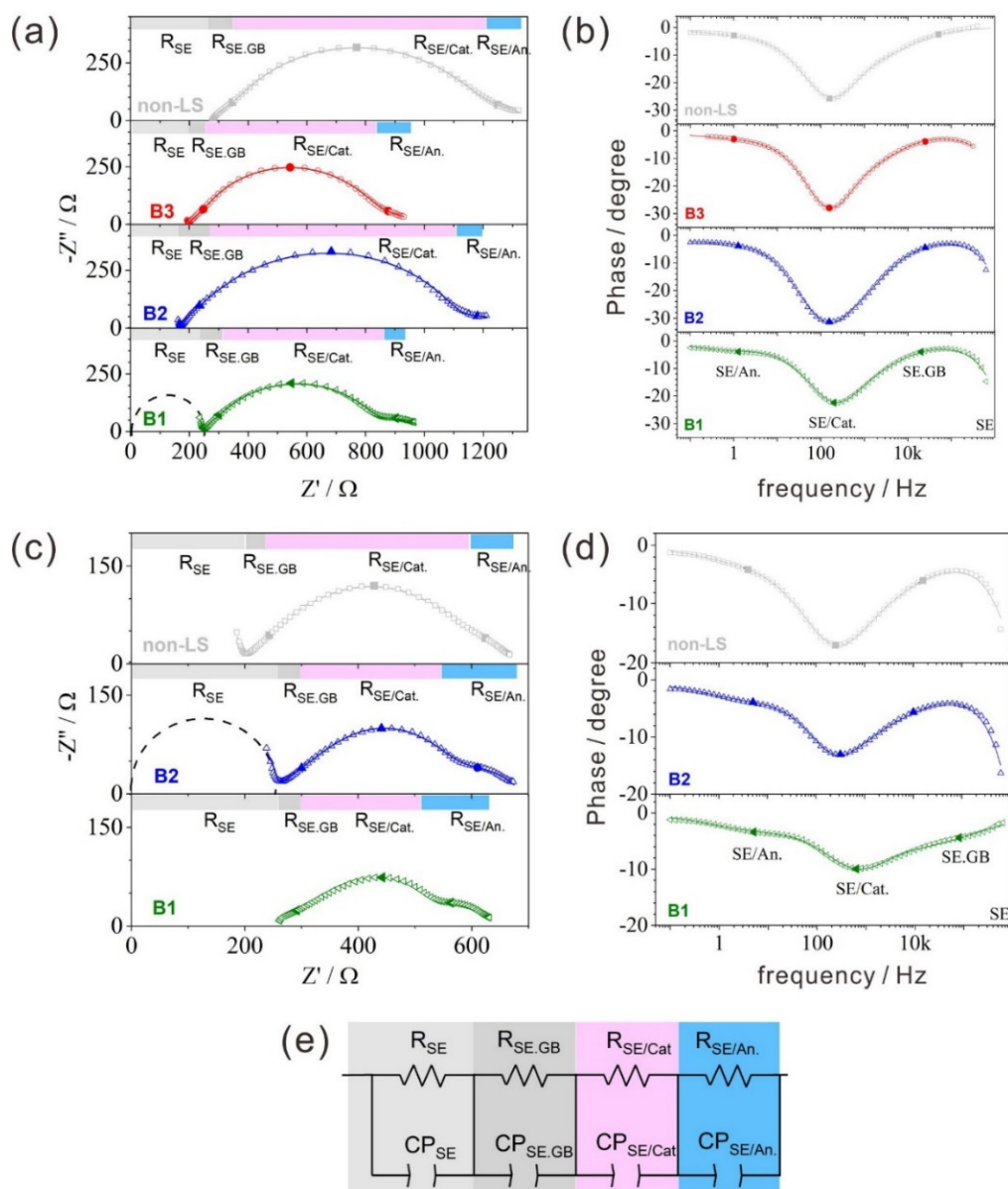


Figure 5. Nyquist and phase plots of the ASSBs using composite electrodes with $80\text{Li}_2\text{S}\cdot20\text{P}_2\text{S}_5$ solid electrolytes prepared via (a,b) simple mixture and (c,d) solution process at the 2nd charge cycle; experimental results (dots); fitting (line). Filled symbols are used to guide the frequency domains in both the Nyquist and Bode plots. (e) Equivalent circuit for impedance fitting. CP is the constant phase element used to simulate the capacitive behavior.

Note that the expected ionic conductivity of the $80\text{Li}_2\text{S}\cdot20\text{P}_2\text{S}_5$ electrolyte through the composite electrode obtained via the solution process is two orders of magnitude lower than that obtained via the simple mixture (Table 1, ionic conductivity of SEs). Furthermore, lower internal resistances and higher initial capacities are obtained by the ASSB using the composite electrode prepared via the solution process (Table 2 and Figure 4). Therefore, the ionic percolation through the battery seems to be of high relevance to reducing the interfacial resistance of the ASSBs, and to achieving high initial capacities. This means that sufficient solid–solid contacts between the active materials and the sulfide SE could have occurred through the composite electrode. Despite the improvement in the electrochemical performance of the ASSB via the solution process, some low reproducibility and slight variation in impedance results between batches remain. However, this issue can be mainly attributed to the low conductivity of the sulfide electrolyte, as will be shown below.

To understand the impact of the lithium-ion conductivity of the sulfide SE on the preparation of the composite electrodes via the solution process, an argyrodite LPSCl with a conductivity of two orders of magnitude greater than that of the 80Li₂S-20P₂S₅ electrolyte was used (Table 1). Figure 6 shows the first charge–discharge curves and cycle performance of the ASSB cells using the composite electrode with the LPSCl solid electrolyte prepared via solution process, as described in Figure 1b.

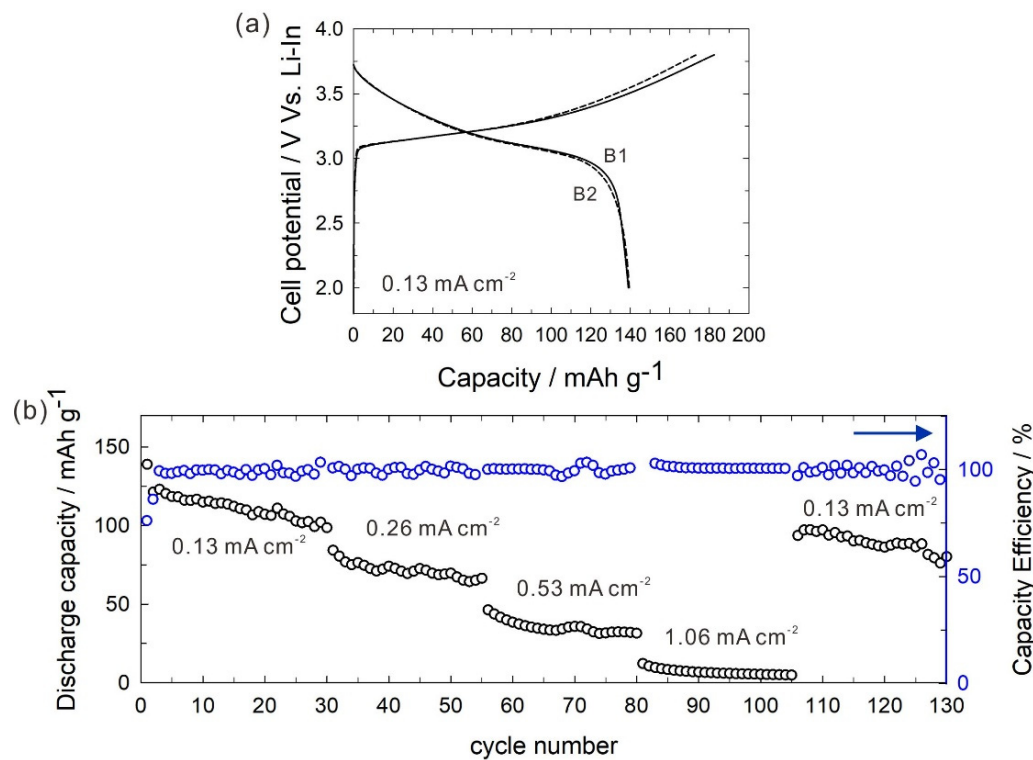


Figure 6. (a) First charge–discharge curves at 2.0 to 3.8 V vs. Li–In alloy (2.6 to 4.2 V vs. Li), and (b) cycle performance of the all-solid-state cells using composite electrodes with LPSCl solid electrolytes prepared via solution process. Capacity efficiency at the end of each current density was removed, since the cells were stopped in order to obtain the electrochemical impedance spectra (Figure 7).

The initial capacity was 140 mAh g⁻¹, which corresponds to 87.5% of the theoretical capacity. Initial low-capacity efficiency can be attributed to the formation of PS₄³⁻, LiCl, and S from the decomposition of the argyrodite solid electrolyte [35,36]. These products work as a passivation layer over subsequent cycles. The high reproducibility of the batches suggests that the enhanced ionic conductivity of SE through the composite electrode and the use of the solution process are effective in improving the transport properties, resulting in the high initial capacity. Capacity fade is observed over cycling (see Figure 6b). The ASSB achieves a discharge capacity of 80 mAh g⁻¹ and capacity efficiency of 95% (130 cycles) after applying high current densities. In the last cycles, the capacity efficiency beyond 100% can be attributed to severe damage in the cell because of the cycle performance.

Figure 7 shows the impedance spectra of ASSBs using composite electrodes with LPSCl prepared via solution process at different cycles after the charging process. The solid lines in Figure 7a–d correspond to the fitting results using the equivalent circuit in Figure 7e, and the fitting results are summarized in Table 3.

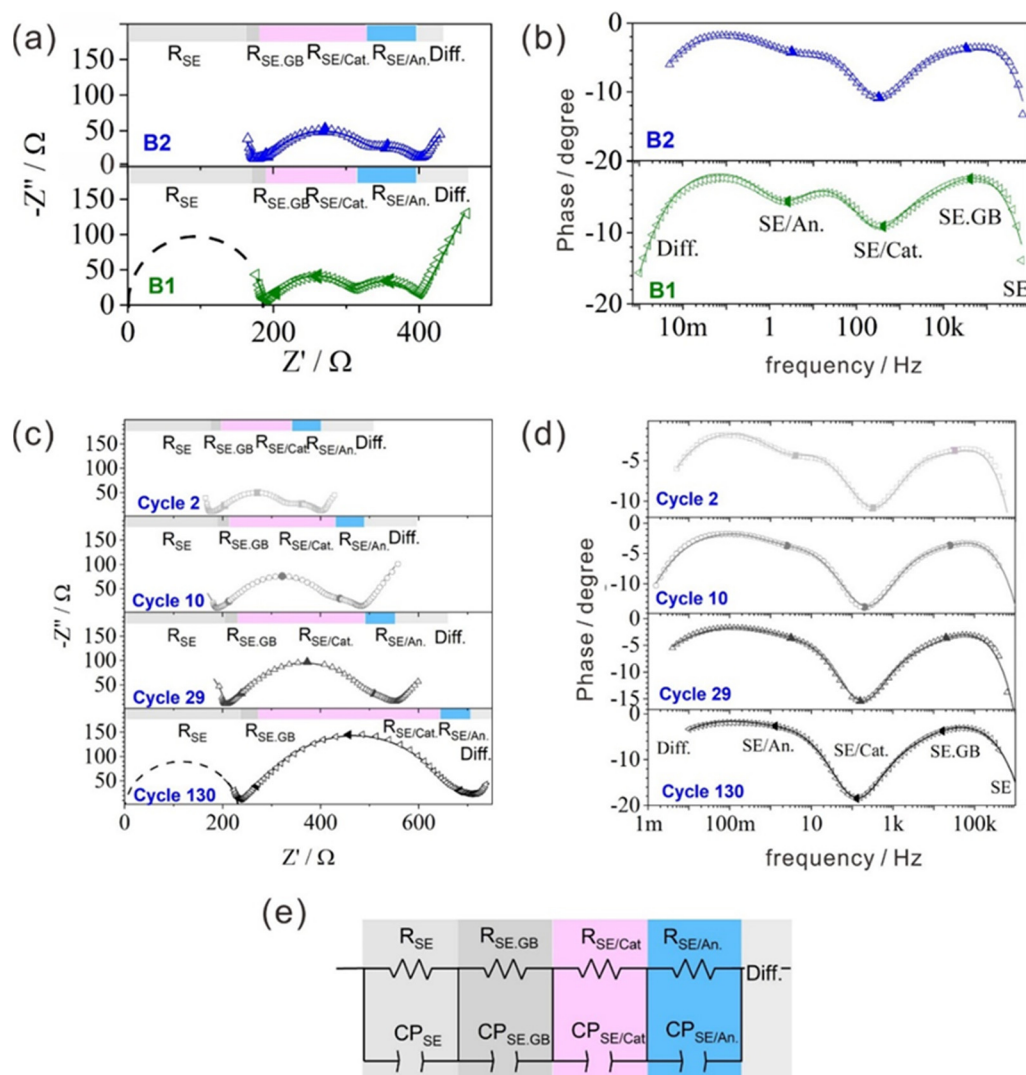


Figure 7. (a,b) Nyquist plot of all-solid-state cells using composite electrodes with Li₆PS₅Cl prepared via solution process at the 2nd charge cycle and (c,d) at different cycles; experimental results (dots); fitting (line). Filled symbols are used to guide the frequency domains in both Nyquist and Bode plots. (e) Equivalent circuit for impedance fitting. CP is the constant phase element used to simulate the capacitive behavior. Diff is simulated with a CP element.

The impedance spectra (Figure 7a,b) show similar contributions to those observed for the composite electrode using 80Li₂S·20P₂S₅ SE (Figure 5c,d). Four characteristic frequencies (see Bode plot) with an equal number of resistances (see Nyquist plot) are distinguished (R_{SE} , $R_{SE,GB}$, $R_{SE/Cat}$, and $R_{SE/An}$), followed by a tail at low frequencies (10 mHz), attributed to the diffusion process (Diff.) through the composite electrode. The total internal resistance (before tail) of the cell was ~400 Ω (Figure 7a,b), which is ~200 Ω lower than that of the ASSB using the composite electrode with 80Li₂S·20P₂S₅. The reduction in the $R_{SE,GB}$ and $R_{SE/Cat}$ (~100–150 Ω) contribute to the reduction in the total resistance, while the R_{SE} (~200 Ω) and $R_{SE/An}$ (~80 Ω) are similar to those reported for the ASSB using the composite electrode with 80Li₂S·20P₂S₅ (Table 2). In this sense, the high ionic conductivity of the LSPCl is crucial to reducing the interfacial resistance and enhancing the ionic percolation through the composite electrode layer prepared via the solution process.

Table 2. Fitting results of impedance spectra (Figure 5) with the composite electrodes with $80\text{Li}_2\text{S}\text{-}20\text{P}_2\text{S}_5$ solid electrolytes prepared via simple mixture and solution processes at the 2nd charge cycle. GOF: goodness of fit (discrepancy between model and experimental values of impedance spectra).

Cathode Composite	R_{SE} (Ω)	$C_{eff,SE}$ (μF)	T_{SE} (s)	$R_{SE,GB}$ (Ω)	$C_{eff,SE,GB}$ (μF)	$T_{SE,GB}$ (s)	$R_{SE/Cat}$ (Ω)	$C_{eff,SE/Cat}$ (μF)	$T_{SE/Cat}$ (s)	$R_{SE/An}$ (Ω)	$C_{eff,SE/An}$ (μF)	$T_{SE/An}$ (s)	GOF
SIMPLE MIXTURE													
Uncoated	277.0	-	-	57.8	0.7	4×10^{-5}	797.0	1.3	1×10^{-3}	245.2	365.9	0.09	2×10^{-5}
B1	244.5	2×10^{-4}	5×10^{-8}	49.1	1.2	6×10^{-5}	543.0	1.4	8×10^{-4}	164.1	1342.8	0.22	6×10^{-5}
B2	167.0	3×10^{-4}	5×10^{-8}	87.2	2.1	2×10^{-4}	858.4	2.0	2×10^{-3}	179.3	5381.6	0.96	6×10^{-5}
B3	195.1	2×10^{-4}	3×10^{-8}	36.9	1.7	6×10^{-5}	525.8	2.7	1×10^{-3}	240.9	168.1	0.04	8×10^{-6}
SOLUTION PROCESS													
Uncoated	189.0	3×10^{-4}	5×10^{-8}	113.7	0.8	9×10^{-5}	295.9	2.6	8×10^{-4}	81.0	732.1	0.06	3×10^{-5}
B1	253.1	-	-	86.4	0.1	5×10^{-6}	191.9	1.2	2×10^{-4}	108.9	253.0	0.03	2×10^{-5}
B2	250.8	3×10^{-4}	6×10^{-8}	114.8	0.6	6×10^{-5}	195.1	3.7	7×10^{-4}	128.2	317.7	0.04	4×10^{-5}

Table 3. Fitting results of impedance spectra (Figure 7) with composite electrodes with LSPCl solid electrolytes prepared via solution process at different charge cycles. GOF: goodness of fit (discrepancy between model and experimental values of impedance spectra).

Electrode Composite–Cycle	R_{SE} (Ω)	$C_{eff,SE}$ (μF)	T_{SE} (s)	$R_{SE,GB}$ (Ω)	$C_{eff,SE,GB}$ (μF)	$T_{SE,GB}$ (s)	$R_{SE/Cat}$ (Ω)	$C_{eff,SE/Cat}$ (μF)	$T_{SE/Cat}$ (s)	$R_{SE/An}$ (Ω)	$C_{eff,SE/An}$ (μF)	$T_{SE/An}$ (s)	T_{Diff} (s)	GOF
B1–2	186.6	3×10^{-4}	5×10^{-8}	19.4	1.4	3×10^{-5}	107.0	3.7	4×10^{-4}	86.0	907.7	0.08	6×10^6	6×10^{-5}
B2–2	171.6	3×10^{-4}	5×10^{-8}	19.4	0.4	7×10^{-6}	150.2	2.0	3×10^{-4}	57.4	1124.2	0.07	4×10^6	3×10^{-5}
B2–10	184.0	2×10^{-4}	3×10^{-8}	23.9	0.5	1×10^{-5}	214.9	2.3	5×10^{-4}	61.1	1263.3	0.08	5×10^6	2×10^{-5}
B2–29	202.0	3×10^{-4}	5×10^{-8}	37.6	0.7	3×10^{-5}	252.6	3.3	8×10^{-4}	56.6	1123.6	0.06	2×10^7	3×10^{-5}
B2–130	231.9	2×10^{-4}	4×10^{-8}	50.0	1.2	6×10^{-5}	379.0	3.3	1×10^{-3}	52.3	2659.2	0.14	5×10^7	1×10^{-5}

The impedance spectra of the ASSBs using composite electrodes with LPSCl prepared via solution process at different cycles (Figure 7c,d, Table 3) show that the RSE/Cat and TSE/Cat are largely affected by cycling at high current densities. RSE/Cat increases to $\sim 379 \Omega$, while TSE/Cat diminishes by one order of magnitude. Both facts could explain the clear capacity fade observed in Figure 6b. The capacity fade of ASSBs has been intensively studied [9,37–39]. The volumetric changes and side reactions at the electrolyte-electrode interface are some of the factors contributing to the battery fade, consistent with the observed tendency of the impedance spectra. The values of R_{SE} , $R_{SE,GB}$, and $T_{SE,GB}$ also slightly increase with the number of cycles, attributed to the volume changes in the cell. $R_{SE,An}$ decreases, because lithium deposition during cycling enhances the interfacial resistance. Diffusion time ($T_{Diff.}$) is the time constant of the CP element used for the simulated diffusion process, as described by Bisquert et al. [40,41]) gradually increases with the number of cycles, showing that lithium mobility decreases strongly during the half-cell cycling. In general terms, the increase in the interfacial resistances suggests that a degradation process during cycling takes place mainly in the electrode composite layer, increasing diffusion time ($T_{Diff.}$) and charge-transfer resistance ($R_{SE/Cat}$). Therefore, the LS coating does not confer sufficient protection to prevent interfacial reactions at high current densities and cycle numbers.

Figure 8a shows the cycle performance of the all-solid-state cells using a composite electrode with an LPSC solid electrolyte prepared via solution process at charge-end voltages from 3.8 to 4.4 V vs. a Li-In alloy (up 5 V vs. Li). The capacity fade of the ASSB is observed during the first 30 cycles, achieving 99 mAh g^{-1} . The discharge capacity slightly increases, reaching 104, 107, 113, 120, and 105 mAh g^{-1} at 3.9, 4.0, 4.1, 4.3, and 4.4 V, respectively. The capacity retention after 10 cycles in each charge-end voltage reaches 96, 98, 97, 91, and 91% (9th cycle) for 3.9, 4.0, 4.1, 4.3, and 4.4 V, respectively. In contrast to the cycle performance of the ASSB at high current densities, the cycle performance at different charge-end voltages suggests that possible interfacial reactions are promoted more at higher potentials. Signals of possible degradation of the cell are observed at the highest potential of 4.3 and 4.4 V vs. the Li-In alloy (4.9 and 5 V vs. Li), in which less capacity retention was also observed. Nevertheless, the potentiality of all-solid-state batteries for high-potential operation is undeniable. For reference, Li-ion batteries using NMC suffer dramatic capacity fade after 4.3 V vs. Li [42].

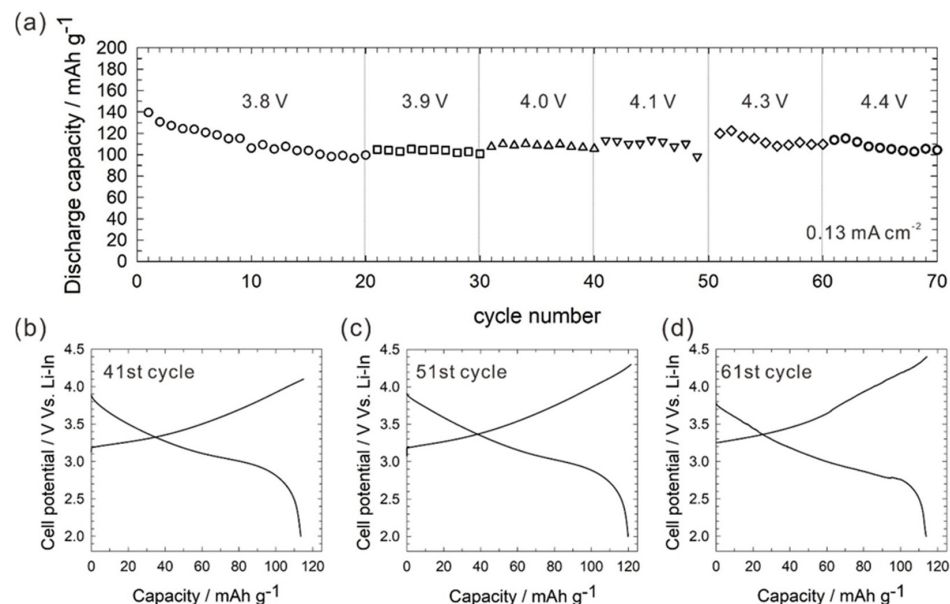


Figure 8. (a) Cycle performance of the all-solid-state cells using composite electrodes with LPSCl SEs prepared via solution process, at charge-end voltages from 3.8 to 4.4 V vs. Li-In alloy (4.4 to 5 V vs. Li). (b–d) Charge–discharge curves performed with charge-end voltages of 4.1, 4.3, and 4.4 V, respectively.

3. Materials and Methods

3.1. Synthesis of Sulfide Solid Electrolytes

The $75\text{Li}_2\text{S}\cdot25\text{P}_2\text{S}_5$ and $80\text{Li}_2\text{S}\cdot20\text{P}_2\text{S}_5$ (mol%) solid electrolytes were prepared via ball milling [43]. The mixture of Li_2S (Mitsuwa Chemical (Cavite, Philippines), 99.9%) and P_2S_5 (Aldrich (St. Louis, MO, USA), 99%) was put into a ZrO_2 pot (volume = 45 mL) with 4 mm diameter ZrO_2 balls (500 balls), and was ball-milled in a PULVERISETTE (Fritsch, Idar-Oberstein, Germany) at 510 rpm (20 h). The $\text{Li}_6\text{PS}_5\text{Cl}$ solid electrolyte was prepared following the procedure reported in [43]. Mechanical milling was conducted using Li_2S , P_2S_5 , and LiCl (Sigma-Aldrich (St. Louis, MO, USA), 99.9%), with 10 mm diameter ZrO_2 balls (15 balls), in a 45 mL ZrO_2 pot at 600 rpm (20 h). For the preparation of sulfide SE solutions, the as-synthesized $80\text{Li}_2\text{S}\cdot20\text{P}_2\text{S}_5$ and $\text{Li}_6\text{PS}_5\text{Cl}$ powders were dissolved in a mixture of ethyl acetate and ethanol (0.1 g mL^{-1}) as described in [43]. The solution was heated at 150°C under a vacuum to remove the solvents.

3.2. Preparation of $\text{Li}_2\text{O}\text{-SiO}_2$ (LS)-Coated NMC

Amorphous $\text{Li}_2\text{O}\text{-SiO}_2$ was prepared via sol-gel process, as described in [44]. Briefly, lithium ethoxide (LiET, 99.9%, High Purity Chemicals, Tokyo, Japan) and tetraethoxysilane (TEOS, Shin-Etsu Chemical, Tokyo, Japan) were used as precursors. Ethanol (99.5%, Wako Pure Chemical, Osaka, Japan) and HCl aqueous solution (Wako Pure Chemical, Osaka, Japan) were used as the solvent and catalyst, respectively. First, TEOS was dissolved in ethanol, and then the catalyst (0.1 wt%) was added dropwise. Later, a LiET solution was added to the prehydrolyzed TEOS solution, and then the mixture was stirred (1 h). Then, lithium silicate sol (up to 10 wt%) was mixed with NMC particles in a mortar, using ethanol to homogenize it. Finally, a heat treatment of 350°C for 30 min was used to consolidate the coating on the NMC particles.

3.3. Preparation of Composite Electrodes

The NMC active material, sulfide SE ($80\text{Li}_2\text{S}\cdot20\text{P}_2\text{S}_5$), and vapor-grown carbon fiber (VGCF, Showa Denko, Japan) were used to prepare the composite electrodes. The weight ratio of NMC:SE:VGCF was 69:29:2. In the composite electrode prepared via simple mixture (Figure 1a), the materials (NMC, SE, and VGCF) were mixed for a few minutes in a mortar. In preparation of the composite electrodes via the solution process (Figure 1b), the NMC and carbon were dispersed in the sulfide SE solution and mixed using a vortex mixer at 2800 rpm (AS ONE test tube shakers, Japan); this last step was used to make the slurry homogeneous. Then, the slurry was heated at 150°C under a vacuum to remove solvents.

3.4. Assembly of All-Solid-State Batteries (ASSBs)

ASSB cells were constructed using $75\text{Li}_2\text{S}\cdot25\text{P}_2\text{S}_5$ solid electrolytes and Li-In alloy as the separator and anode, respectively. The $75\text{Li}_2\text{S}\cdot25\text{P}_2\text{S}_5$ shows a slightly lower Young's modulus than $80\text{Li}_2\text{S}\cdot20\text{P}_2\text{S}_5$ and, therefore, it was selected as the SE separator in the ASSBs [45]. The composite electrode (10 mg) and $75\text{Li}_2\text{S}\cdot25\text{P}_2\text{S}_5$ solid electrolyte (80 mg) formed a bilayer pellet ($\varphi = 10 \text{ mm}$) via pressing under 360 MPa at room temperature. On the opposite side of the composite electrode, indium foil was attached to the $75\text{Li}_2\text{S}\cdot25\text{P}_2\text{S}_5$ solid electrolyte separator by pressing under 120 MPa. Then, the cells were pressed using two stainless steel rods (current collectors) for both the positive composite electrode and negative Li-In alloy electrode.

3.5. Characterization

X-ray diffraction patterns (XRD, MiniFlex 600, Rigaku (Tokyo, Japan)) were collected in the 2θ range between 10° and 70° , at a step size of 0.02° . The morphology of the NMC and composite electrodes was investigated via scanning electron microscopy (SEM, JIB-4600F MultiBeam SEM-FIB) and transmission electron microscopy (TEM, JEOL JEM-2010). The charge-discharge performance of the cells (580 battery type system, Scribner Associates) was evaluated under a constant current (0.13 to $1 \text{ mA}\cdot\text{cm}^{-2}$), with cutoff voltages of 2.0 V to

3.8 V (up to 4.4 V) vs. Li–In at room temperature. The reported capacity of the batteries was normalized to active material weight (69 mg). Electrochemical impedance spectroscopy (EIS, SI 1260, SI 1280 Solartron) was evaluated in the frequency range from 1 MHz to 1 mHz, at an amplitude perturbation of 30 mV. In the case of solid electrolytes, the ionic conductivity was evaluated via EIS in the frequency range of 0.1 MHz to 200 Hz using pelletized SE samples (80 mg, 360 MPa), at an amplitude perturbation of 10 mV.

4. Conclusions

Composite electrodes containing LS-coated NMC, a sulfide solid electrolyte, and carbon additives were prepared via two procedures: simple mixture, and solution process. An amorphous LS coating with a thickness around 9 nm was used. The solution process allowed us to obtain an enhanced solid–solid contact between the sulfide SE and the active material particles (confirmed by SEM), resulting in low internal resistances and high initial capacities. The use of the LS protective coating reduced the interface resistance $R_{SE/Cat}$, proving that the LS coating was effective in blocking the initial interfacial reactions. The use of high ionic conductor argyrodite-type LPSCl in the composite electrode layer enhanced the ionic percolation through the composite electrode, resulting in a high initial capacity of 140 mAh g^{-1} , and enabling the ASSBs’ use at high potentials. The charge-transfer resistance between the solid electrolyte and the electrode materials is the main parameter derived from the impedance analysis to understand the initial ASSB status. This resistance shows high values due to insufficient solid–solid contacts between the active material and the sulfide electrolyte, and low ionic conductivity of the ionic conductor in the composite electrode layer.

Author Contributions: S.G., K.N. and F.A.V. are co-first authors and therefore, they can cite the paper in the preferred order if desired. Conceptualization, supervision and funding acquisition, N.C.R.-N., A.M., J.A.C. and K.T.; investigation, S.G., K.N., F.A.V., Y.F. and Y.W.; writing—original draft preparation, S.G., K.N. and F.A.V.; writing—review and editing, all authors. All authors have read and agreed to the published version of the manuscript.

Funding: The present work was partially supported by the Japan Science and Technology Agency (JST), the Advanced Low-Carbon Technology Research and Development Program (ALCA), the Specially Promoted Research for Innovative Next-Generation Batteries (SPRING) project, and the Colombian Ministry of Science, Technology, and Innovation “Minciencias” under the project 1115-745-58653, contract number FP44842-13-2017.

Institutional Review Board Statement: Not applicable.

Informed Consent Statement: Not applicable.

Acknowledgments: The present work was partially supported by the Japan Science and Technology Agency (JST), the Advanced Low-Carbon Technology Research and Development Program (ALCA), and the Specially Promoted Research for Innovative Next-Generation Batteries (SPRING) project. Sara Giraldo, F.A. Vásquez, and J. Calderón would like to thank the Colombian Ministry of Science, Technology, and Innovation “Minciencias”, TRONEX S.A.S., and the University of Antioquia for their support of project 1115-745-58653, contract number FP44842-13-2017. The TEM and SEM analyses were carried out with JIB-4600F at the “Joint-Use Facilities: Laboratory of Nano-Micro Material Analysis”, Hokkaido University, supported by the “Material Analysis and Structure Analysis Open Unit (MASAOU)”.

Conflicts of Interest: The authors declare no conflict of interest.

References

1. Zhou, L.; Zhang, K.; Hu, Z.; Tao, Z.; Mai, L.; Kang, Y.M.; Chou, S.L.; Chen, J. Recent Developments on and Prospects for Electrode Materials with Hierarchical Structures for Lithium-Ion Batteries. *Adv. Energy Mater.* **2018**, *8*, 1–23. [[CrossRef](#)]
2. Baster, D.; Paziak, P.; Zi, M.; Wazny, G.; Molenda, J. LiNi_{0.6}Co_{0.4-z}Ti_zO₂-New cathode materials for Li-ion batteries. *Solid State Ion.* **2018**, *320*, 118–125. [[CrossRef](#)]
3. Xiayin, Y.; Bingxin, H.; Jingyun, Y.; Gang, P.; Zhen, H.; Chao, G.; Deng, L.; Xiaoxiong, X. All-solid-state lithium batteries with inorganic solid electrolytes: Review of fundamental. *Chin. Phys. B* **2019**, *25*, 1–14.

4. Deng, S.; Sun, Q.; Li, M.; Adair, K.; Yu, C.; Li, J.; Li, W.; Fu, J.; Li, X.; Li, R.; et al. Insight into cathode surface to boost the performance of solid-state batteries. *Energy Storage Mater.* **2021**, *35*, 661–668. [[CrossRef](#)]
5. Zheng, F.; Kotobuki, M.; Song, S.; Lai, M.O.; Lu, L. Review on solid electrolytes for all-solid-state lithium-ion batteries. *J. Power Sources* **2018**, *389*, 198–213. [[CrossRef](#)]
6. Takada, K.; Ohta, N.; Zhang, L.; Xu, X.; Thi Hang, B.; Ohnishi, T.; Osada, M.; Sasaki, T. Interfacial phenomena in solid-state lithium battery with sulfide solid electrolyte. *Solid State Ion.* **2012**, *225*, 594–597. [[CrossRef](#)]
7. Richards, W.D.; Miara, L.J.; Wang, Y.; Kim, J.C.; Ceder, G. Interface stability in solid-state batteries. *Chem. Mater.* **2016**, *28*, 266–273. [[CrossRef](#)]
8. Sumita, M.; Tanaka, Y.; Ikeda, M.; Ohno, T. Charged and discharged states of cathode/sulfide electrolyte interfaces in all-solid-state lithium ion batteries. *J. Phys. Chem. C* **2016**, *120*, 13332–13339. [[CrossRef](#)]
9. Sakuda, A.; Hayashi, A.; Tatsumisago, M. Interfacial observation between LiCoO_2 electrode and $\text{Li}_2\text{S}-\text{P}_2\text{S}_5$ solid electrolytes of all-solid-state lithium secondary batteries using transmission electron microscopy. *Chem. Mater.* **2010**, *22*, 949–956. [[CrossRef](#)]
10. Kwak, H.W.; Park, Y.J. Cathode coating using $\text{LiInO}_2-\text{LiI}$ composite for stable sulfide-based all-solid-state batteries. *Sci. Rep.* **2019**, *9*, 8099. [[CrossRef](#)]
11. Deng, S.; Sun, Y.; Li, X.; Ren, Z.; Liang, J.; Doyle-Davis, K.; Liang, J.; Li, W.; Banis, M.N.; Sun, Q.; et al. Eliminating the Detrimental Effects of Conductive Agents in Sulfide-Based Solid-State Batteries. *ACS Energy Lett.* **2020**, *5*, 1243–1251. [[CrossRef](#)]
12. Wu, J.; Shen, L.; Zhang, Z.; Liu, G.; Wang, Z.; Zhou, D.; Wan, H.; Xu, X.; Yao, X. All-Solid-State Lithium Batteries with Sulfide Electrolytes and Oxide Cathodes. *Electrochem. Energy Rev.* **2021**, *4*, 101135. [[CrossRef](#)]
13. Woo, J.H.; Trevey, J.E.; Cavanagh, A.S.; Choi, Y.S.; Kim, S.C.; George, S.M.; Oh, K.H.; Lee, S.-H. Nanoscale interface modification of LiCoO_2 by Al_2O_3 atomic layer deposition for solid-state Li batteries. *J. Electrochem. Soc.* **2012**, *159*, A1120–A1124. [[CrossRef](#)]
14. Li, X.; Liang, M.; Sheng, J.; Song, D.; Zhang, H.; Shi, X.; Zhang, L. Constructing double buffer layers to boost electrochemical performances of NCA cathode for ASSLB. *Energy Storage Mater.* **2019**, *18*, 100–106. [[CrossRef](#)]
15. Yubuchi, S.; Ito, Y.; Matsuyama, T.; Hayashi, A.; Tatsumisago, M. 5 V class $\text{LiNi}_{0.5}\text{Mn}_{1.5}\text{O}_4$ positive electrode coated with Li_3PO_4 thin film for all-solid-state batteries using sulfide solid electrolyte. *Solid State Ion.* **2016**, *285*, 79–82. [[CrossRef](#)]
16. Kim, J.; Kim, M.; Noh, S.; Lee, G.; Shin, D. Enhanced electrochemical performance of surface modified LiCoO_2 for all-solid-state lithium batteries. *Ceram. Int.* **2016**, *42*, 2140–2146. [[CrossRef](#)]
17. Miura, A.; Rosero-Navarro, N.C.; Sakuda, A.; Tadanaga, K.; Phuc, N.H.H.; Matsuda, A.; Machida, N.; Hayashi, A.; Tatsumisago, M. Liquid-phase syntheses of sulfide electrolytes for all-solid-state lithium battery. *Nat. Rev. Chem.* **2019**, *3*, 189–198. [[CrossRef](#)]
18. Tadanaga, K.; Rosero-Navarro, N.C.; Miura, A. Wet Chemical Processes for the Preparation of Composite Electrodes in All-Solid-State Lithium Battery. In *Next Generation Batteries: Realization of High Energy Density Rechargeable Batteries*; Kanamura, K., Ed.; Springer: Singapore, 2021; pp. 85–92.
19. Teragawa, S.; Aso, K.; Tadanaga, K.; Hayashi, A.; Tatsumisago, M. Liquid-phase synthesis of a Li_3PS_4 solid electrolyte using N-methylformamide for all-solid-state lithium batteries. *J. Mater. Chem. A* **2014**, *2*, 5095–5099. [[CrossRef](#)]
20. Yubuchi, S.; Teragawa, S.; Aso, K.; Tadanaga, K.; Hayashi, A.; Tatsumisago, M. Preparation of high lithium-ion conducting $\text{Li}_6\text{PS}_5\text{Cl}$ solid electrolyte from ethanol solution for all-solid-state lithium batteries. *J. Power Sources* **2015**, *293*, 941–945. [[CrossRef](#)]
21. Park, K.H.; Oh, D.Y.; Choi, Y.E.; Nam, Y.J.; Han, L.L.; Kim, J.Y.; Xin, H.L.; Lin, F.; Oh, S.M.; Jung, Y.S. Solution-processable glass $\text{LiI}-\text{Li}_4\text{SnS}_4$ superionic conductors for all-solid-state Li-ion batteries. *Adv. Mater.* **2016**, *28*, 1874–1883. [[CrossRef](#)]
22. Choi, Y.E.; Park, K.H.; Kim, D.H.; Oh, D.Y.; Kwak, H.R.; Lee, Y.G.; Jung, Y.S. Coatable Li_4SnS_4 Solid Electrolytes Prepared from Aqueous Solutions for All-Solid-State Lithium-Ion Batteries. *ChemSusChem* **2017**, *10*, 2605–2611. [[CrossRef](#)] [[PubMed](#)]
23. Chida, S.; Miura, A.; Rosero-Navarro, N.C.; Higuchi, M.; Phuc, N.H.H.; Muto, H.; Matsuda, A.; Tadanaga, K. Liquid-phase synthesis of $\text{Li}_6\text{PS}_5\text{Br}$ using ultrasonication and application to cathode composite electrodes in all-solid-state batteries. *Ceram. Int.* **2017**, *44*, 742–746. [[CrossRef](#)]
24. Yao, X.; Liu, D.; Wang, C.; Long, P.; Peng, G.; Hu, Y.-S.; Li, H.; Chen, L.; Xu, X. High-Energy All-Solid-State Lithium Batteries with Ultralong Cycle Life. *Nano Lett.* **2016**, *16*, 7148–7154. [[CrossRef](#)] [[PubMed](#)]
25. Zhang, Q.; Mwizerwa, J.P.; Wan, H.L.; Cai, L.T.; Xu, X.X.; Yao, X.Y. $\text{Fe}_3\text{S}_4@ \text{Li}_7\text{P}_3\text{S}_{11}$ nanocomposites as cathode materials for all-solid-state lithium batteries with improved energy density and low cost. *J. Mater. Chem. A* **2017**, *5*, 23919–23925. [[CrossRef](#)]
26. Xu, R.C.; Wang, X.L.; Zhang, S.Z.; Xia, Y.; Xia, X.H.; Wu, J.B.; Tu, J.P. Rational coating of $\text{Li}_7\text{P}_3\text{S}_{11}$ solid electrolyte on MoS_2 electrode for all-solid-state lithium ion batteries. *J. Power Sources* **2018**, *374*, 107–112. [[CrossRef](#)]
27. Famprikis, T.; Canepa, P.; Dawson, J.A.; Islam, M.S.; Masquelier, C. Fundamentals of inorganic solid-state electrolytes for batteries. *Nat. Mater.* **2019**, *18*, 1278–1291. [[CrossRef](#)]
28. Zhao, E.; Liu, X.; Zhao, H.; Xiao, X.; Hu, Z. Ion conducting Li_2SiO_3 -coated lithium-rich layered oxide exhibiting high rate capability and low polarization. *Chem. Commun.* **2015**, *51*, 9093–9096. [[CrossRef](#)]
29. Sakuda, A.; Kitaura, H.; Hayashi, A.; Tadanaga, K.; Tatsumisago, M. Improvement of High-Rate Performance of All-Solid-State Lithium Secondary Batteries Using LiCoO_2 Coated with $\text{Li}_2\text{O}-\text{SiO}_2$ Glasses. *Electrochim. Solid-State Lett.* **2007**, *11*, A1. [[CrossRef](#)]
30. Ohta, N.; Takada, K.; Sakaguchi, I.; Zhang, L.; Ma, R.; Fukuda, K.; Osada, M.; Sasaki, T. LiNbO_3 -coated LiCoO_2 as cathode material for all solid-state lithium secondary batteries. *Electrochim. Commun.* **2007**, *9*, 1486–1490. [[CrossRef](#)]
31. Hirschorn, B.; Orazem, M.E.; Tribollet, B.; Vivier, V.; Frateur, I.; Musiani, M. Electrochimica Acta Determination of effective capacitance and film thickness from constant-phase-element parameters. *Electrochim. Acta J.* **2010**, *55*, 6218–6227. [[CrossRef](#)]

32. Calpa, M.; Rosero-Navarro, N.C.; Miura, A.; Tadanaga, K. Electrochemical performance of bulk-type all-solid-state batteries using small-sized Li₇P₃S₁₁ solid electrolyte prepared by liquid phase as the ionic conductor in the composite cathode. *Electrochim. Acta* **2019**, *296*, 473–480. [[CrossRef](#)]
33. Ohno, S.; Bernges, T.; Buchheim, J.; Duchardt, M.; Hatz, A.-K.; Kraft, M.A.; Kwak, H.; Santhosha, A.L.; Liu, Z.; Minafra, N.; et al. How Certain Are the Reported Ionic Conductivities of Thiophosphate-Based Solid Electrolytes? An Interlaboratory Study. *ACS Energy Lett.* **2020**, *5*, 910–915. [[CrossRef](#)]
34. Koerver, R.; Aygün, I.; Leichtweiss, T.; Dietrich, C.; Zhang, W.; Binder, J.O.; Hartmann, P.; Zeier, W.G.; Janek, J. Capacity Fade in Solid-State Batteries: Interphase Formation and Chemomechanical Processes in Nickel-Rich Layered Oxide Cathodes and Lithium Thiophosphate Solid Electrolytes. *Chem. Mater.* **2017**, *29*, 5574–5582. [[CrossRef](#)]
35. Schwietert, T.K.; Arszelewska, V.A.; Wang, C.; Yu, C.; Vasileiadis, A.; de Klerk, N.J.J.; Hageman, J.; Hupfer, T.; Kerkamm, I.; Xu, Y.; et al. Clarifying the relationship between redox activity and electrochemical stability in solid electrolytes. *Nat. Mater.* **2020**, *19*, 428–435. [[CrossRef](#)] [[PubMed](#)]
36. Tan, D.H.S.; Wu, E.A.; Nguyen, H.; Chen, Z.; Marple, M.A.T.; Doux, J.M.; Wang, X.; Yang, H.; Banerjee, A.; Meng, Y.S. Elucidating Reversible Electrochemical Redox of Li₆PS₅C₁ Solid Electrolyte. *ACS Energy Lett.* **2019**, *4*, 2418–2427. [[CrossRef](#)]
37. Noh, H.-J.; Youn, S.; Yoon, C.S.; Sun, Y.-K. Comparison of the structural and electrochemical properties of layered Li[Ni_xCoyMnz]O₂ ($x = 1/3$, 0.5, 0.6, 0.7, 0.8 and 0.85) cathode material for lithium-ion batteries. *J. Power Sources* **2013**, *233*, 121–130. [[CrossRef](#)]
38. Zhang, Q.; Cao, D.; Ma, Y.; Natan, A.; Aurora, P.; Zhu, H. Sulfide-Based Solid-State Electrolytes: Synthesis, Stability, and Potential for All-Solid-State Batteries. *Adv. Mater.* **2019**, *31*, 1901131. [[CrossRef](#)]
39. Lou, S.; Liu, Q.; Zhang, F.; Liu, Q.; Yu, Z.; Mu, T.; Zhao, Y.; Borovilas, J.; Chen, Y.; Ge, M.; et al. Insights into interfacial effect and local lithium-ion transport in polycrystalline cathodes of solid-state batteries. *Nat. Commun.* **2020**, *11*, 1–10. [[CrossRef](#)] [[PubMed](#)]
40. Bisquert, J.; Garcia-belmonte, G.; Bueno, P.; Longo, E.; Bulhoes, L.O. Impedance of constant phase element (CPE)-blocked diffusion in film electrodes. *J. Electroanal. Chem.* **1998**, *452*, 229–234. [[CrossRef](#)]
41. Bisquert, J.; Garcia-Belmonte, G.; Fabregat-Santiago, F.; Bueno, P.R. Theoretical models for ac impedance of finite diffusion layers exhibiting low frequency dispersion. *J. Electroanal. Chem.* **1999**, *475*, 152–163. [[CrossRef](#)]
42. Jung, R.; Metzger, M.; Maglia, F.; Stinner, C.; Gasteiger, H.A. Oxygen Release and Its Effect on the Cycling Stability of LiNixMnyCozO₂ (NMC) Cathode Materials for Li-Ion Batteries. *J. Electrochem. Soc.* **2017**, *164*, A1361–A1377. [[CrossRef](#)]
43. Hayashi, A.; Hama, S.; Morimoto, H.; Tatsumisago, M.; Minami, T. Preparation of Li₂S-P₂S₅ amorphous solid electrolytes by mechanical milling. *J. Am. Ceram. Soc.* **2004**, *84*, 477–479. [[CrossRef](#)]
44. Rosero-Navarro, N.C.; Kajura, R.; Jalem, R.; Tateyama, Y.; Miura, A.; Tadanaga, K. Significant Reduction in the Interfacial Resistance of Garnet-Type Solid Electrolyte and Lithium Metal by a Thick Amorphous Lithium Silicate Layer. *ACS Appl. Energy Mater.* **2020**, *3*, 5533–5541. [[CrossRef](#)]
45. Sakuda, A.; Yamamoto, M.; Nose, M.; Kato, A.; Hayashi, A.; Tatsumisago, M. Mechanical properties of sul fi de glasses in all-solid-state batteries. *J. Ceram. Soc. Jpn.* **2018**, *126*, 719–727. [[CrossRef](#)]